Journal of Design Against Fatigue
https://minerva-aset.com/JDAF

MINERVA ASET ISSN 2976-940X

Low cycle fatigue behavior and life prediction of a directionally solidified alloy

B. Salehnasab [a*], S. Hashem-Sharifi [b]

[a] *Department of Mechanical Engineering, Auburn University, Auburn, AL 36849, USA*
[b] *Department of Continuum Mechanics and Structural Analysis, University Carlos III of Madrid, Avda. de la Universidad, 30, 28911 Leganés, Madrid, Spain*

P A P E R I N F O

Paper history:
Received 11 November 2023
Received in revised form 7 December 2023
Accepted 8 December 2023

Keywords:
Low cycle fatigue
Directionally-solidified alloy
Coffin-Manson model
Hysteresis energy criterion

A B S T R A C T

Alloys used in engines are subjected to challenging environments characterized by thermal and mechanical cyclic loadings during start-up and shut-down processes. These conditions can significantly increase the occurrence of fatigue failure mechanisms. Therefore, this study focuses on investigating the low cycle fatigue (LCF) behavior of directionally-solidified alloy at two distinct temperatures, namely 600 °C and 800 °C. Strain-controlled LCF tests were conducted at the specified temperatures, utilizing constant total strain amplitudes of 0.4%, 0.6%, 0.8%, and 1% under a totally reversed loading ratio (R = -1). The Coffin-Manson model, based on plastic deformation, along with a hysteresis energy-based criterion model, were employed to predict and evaluate fatigue life and LCF behavior. Notably, the hysteresis energy and Coffin-Manson models exhibited superior capability in predicting LCF life at 800 °C compared to 600 °C.

doi: *https://doi.org/10.62676/ygye8n63*

1. INTRODUCTION

In engines alloys and superalloys are used to achieve better efficiency and to attempt to optimize performance and efficiency. To control the energy requirement of engines, more start-up and shut-down operations are necessary. Throughout the start-up operation, the external surface of the rotary component heats up before the internal surface. Then, compressive stress on the external surface is created. Throughout the shut-down operation, the external surface cools down faster. Then, tensile stress on the external surface is created [1]. Furthermore, the microstructure of the superalloys unavoidably becomes degraded due to operating at elevated temperatures and high rotation speeds [2,3]. Therefore, flexibility also becomes more important [4]. First-generation Ni-base superalloys have been broadly improved over time; and finally, as a solution to continual requisitions for higher outputs of engines, single-crystal, and directionally-solidified superalloys were developed [5,6]. Due to their notable thermo-mechanical resistance, single-crystal and directionally-solidified Nickel-base superalloys are generally used as a material for hot section components of heavy duty engines [7,8]. The directionally-solidified is one of the many alloys which are vastly used in the components of heavy duty engines [9,10]. The appropriate mechanical properties at high temperatures are a consequence of the γ′ precipitates in the matrix of the γ phase [11,12]. The γ and γ′ phases are generally solid-solution strengthened. After accumulating damage during fatigue exploitations, the parameters that are of high importance include the microstructural ones such as volume fraction and coherency strains between γ-γ′ and so on [13,14]. Numerous damage mechanisms occur in engines, which can cause the failure of blades and nozzles, such as low cycle and high cycle fatigue, creep, thermo-mechanical fatigue (TMF), corrosion, foreign object damage, erosion, and oxidation [15–19]. Metal fatigue is one of the serious mechanical damages in rotary equipment [20]. Due to the engine start-up and shut-down processes as well as cooling by the axial air compressor, hot-section components of a heavy duty engine experience significant thermal fluctuations, resulting in localized and

*Corresponding Author Email: ***bzs0127@auburn.edu*** (Behnam Salehnasab)

Cite this article as: Authors names separated by comma in Cambria 8, Title of the article in Cambria 8, ***Journal of Design Against Fatigue,*** Vol. 2, No. 1, (2024) 1-10, *https://doi.org/10.62676/ygye8n63*

small plastic strains [21]. Thus, these components are designed such that they can be resistant to low cycle fatigue. To guarantee adequate creep and fatigue resistance, the directionally-solidified nickel-based alloy materials are selected by manufacturers. The low cycle fatigue failure can lead to trip the heavy duty engines and economic loss markedly in gas transmission stations and power plants, while this can also cause catastrophic damage to aero-engines [22–24]. Generally, stress-strain and temperature fields are the basis of the models used for LCF calculation [25]. Low cycle fatigue in equiaxed and directionally-solidified Ni-based superalloys has been studied widely over the past two decades. S.M. Seo et al. [26] investigated the low cycle fatigue behavior of Ni-based super-alloy CM247LC at 760 °C. Antolovich et al. [27] investigated the low cycle fatigue behavior of René 80 at two temperatures of 871 and 982 °C. It was found that when frequency decreased the fatigue life was increased. He et al. [28] investigated the influence of temperature on the low cycle fatigue behavior of a directionally-solidified solidified Mar-M200 superalloy from 550 to 850 °C. It was found that the deformation of γ′ becomes an anomaly and some secondary precipitates can be observed in the matrix by increasing the temperature. He et al. [29] investigated the influence of strain amplitude and temperature on the dislocation of M963 during low cycle fatigue at high temperatures. It was found that the main deformation mode at the temperature between 700 and 800°C was dislocation shearing γ′ precipitates by dislocation pairs and at the temperature between 900 and 950°C was dislocations by-passing γ′ precipitates. Deng et al. [30] studied the damage mechanism and the fatigue behavior of Inconel 718 under TMF and isothermal LCF. It was found that the Coffin-Manson equation can predict S-N results under the test condition, and the hysteresis energy model can be predicted lifetime under the TMF condition. Kashinga et al. [31] investigated the effect of dwell time on the low cycle fatigue of a directionally-solidified solidified Ni-based superalloy using both experimental and computational methods. Mukherjee et al. [32] investigated the LCF behavior of Haynes 282 and its correlation with microstructure at a temperature of 760 °C. Rao et al. [33] investigated the low cycle fatigue behavior of Inconel 617 at room temperature and 750 °C. The results showed the cyclic hardening was occurred and also, once the temperature raised from room temperature to 750 °C the fatigue life is reduced. Zhang et al. [14] investigated the LCF behavior of a nickel-based single-crystal superalloy with an emphasis on the influence of temperature and crystal orientation. It was found LCF lifetime was decreased expressively by changing loading orientation from [001] to [111] or increasing temperature to 825 °C.

The present study aimed to investigate the two different models to predict the isothermal low cycle fatigue behavior in a directionally-solidified solidified alloy in the two temperatures of 600 °C to 800 °C. In this regard, low cycle fatigue life prediction based on a set of LCF experiments was investigated in the study.

2. MATERIALS AND METHODS

2.1. Material Evaluations

The material selected for the current study was a directionally-solidified, which is hafnium (Hf) containing a Ni-base alloy established for heavy duty engines components. The chemical composition and the mechanical properties of the cast directionally-solidified are presented in Table 1. The chemical composition was obtained by using quantometer analysis and the mechanical and physical properties are referred to [34]. The material was produced through vacuum induction melting. The alloy was directionally-solidified into bars of ϕ 22×120 mm. The material under study went through a three-step heat-treatment process. Initially, the material was solution heat-treated at 1250 °C for 2.5 h, followed by cooling. Precipitation of a uniform fine γ/γ′ microstructure has resulted from this step. As the second step, the material was heat-treated at 1080 °C for 4.5 h, which resulted in an optimized distribution size of γ′ precipitates. For aging heat-treatment, the third step was applied at 860 °C for 24 h. The processing and development of a directionally-solidified alloy are reported in Ref. [34]. Generally, in the directionally-solidified and single-crystal Ni-based materials, the mechanical characteristics are extremely dependent on the γ' precipitates' specifications including size, volume fraction, and distribution [35,36]. For the examination of microstructures, the specimens were cut from the casted material through the EDM process for metallographic evaluation and then the standard procedure of polishing was performed on the samples. The etched process was performed with a solution of nitric acid, lactic acid, and hydrogen fluoride regent for a time of 120 s and at a voltage of 7 V. The OLYMPUS optical microscope and a TESCAN FE-SEM (Field Emission Scanning Electron Microscope) were used to examine the fractured surfaces. For this purpose, a rod specimen with dimensions of 15 mm in diameter and 10 mm in length was prepared. For statistical analysis of the metallurgical data of the SEM images an metallographic image processing software (MIP) was used. The optical micrographs of the microstructures in the longitudinal and traverse sections of the grain axis of alloy are shown in Fig. 1(a) and (b), respectively. As can be observed, the microstructure involves both primary and secondary dendrites as well as inter-dendritic regions. In Fig. 1(b), the mean of primary dendrite arm spacing size is 250 μm and the mean of secondary dendrite arm spacing size is 210 μm. Furthermore, some distributed microstructural features like eutectic γ/γ' are observed in the white-colored. The SEM images of the microstructure are shown in Fig. 2. Four EDS points were taken from formed (HF/Ta) C, γ/γ' eutectic phase, γ matrix, and γ', respectively. The EDS results are shown in Fig. 2. As can be seen, the γ' intermetallic phase is distributed in a matrix of γ. The EDS points were taken from eutectic phase, carbide, and matrix, respectively. As can be observed, Co, Cr and W segregated mainly to the dendrite cores, and Al, Ti and Ta generally were found in inter-dendritic regions. The micro-segregation yielded a large chemical heterogeneity between the dendrites and the inter-dendritic regions. Also, continuous carbide phases were observed in grain boundaries. The average γ' precipitate phase fraction was obtained as 62% and the mean size of the γ' precipitate was achieved as 0.5 μm. The grain boundaries consisted of the main percentage of primary γ/γ' eutectic phase and only a small percentage within the grains.

TABLE 1. Chemical composition and mechanical properties of the DS alloy at the room condition

Chemical composition (wt%)							
Ni	**Al**	**Co**	**Cr**	**Fe**	**Hf**	**Mo**	**Nb**
Rem	5.73	9.32	8.09	0.02	1.35	0.51	0.01
Si	**Mn**	**Ta**	**Ti**	**W**	**B**	**Zr**	
0.01	0.01	3.23	0.71	9.66	0.015	0.009	

Mechanical properties				
Density (g/cm3)	**Modulus of Elasticity (GPa)**	**Offset Yield Strength at 0.2% (MPa)**	**Ultimate Tensile Strength (MPa)**	**Degree of work hardening (σ_{UTS}/σ_{YS})**
8.3	140	970	1150	1.32

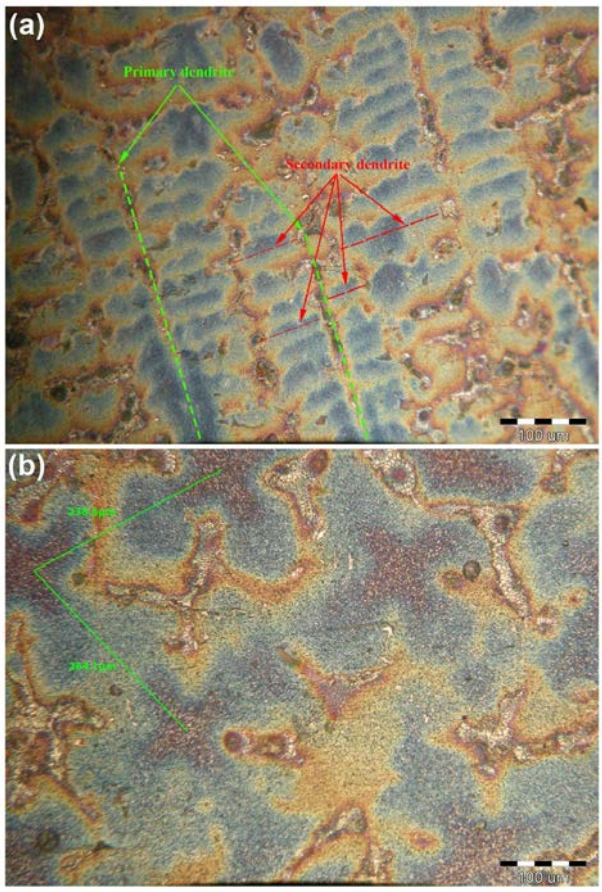

Figure 1. Optical microscopy of the DS alloy: a) longitudinal section; b) transverse section

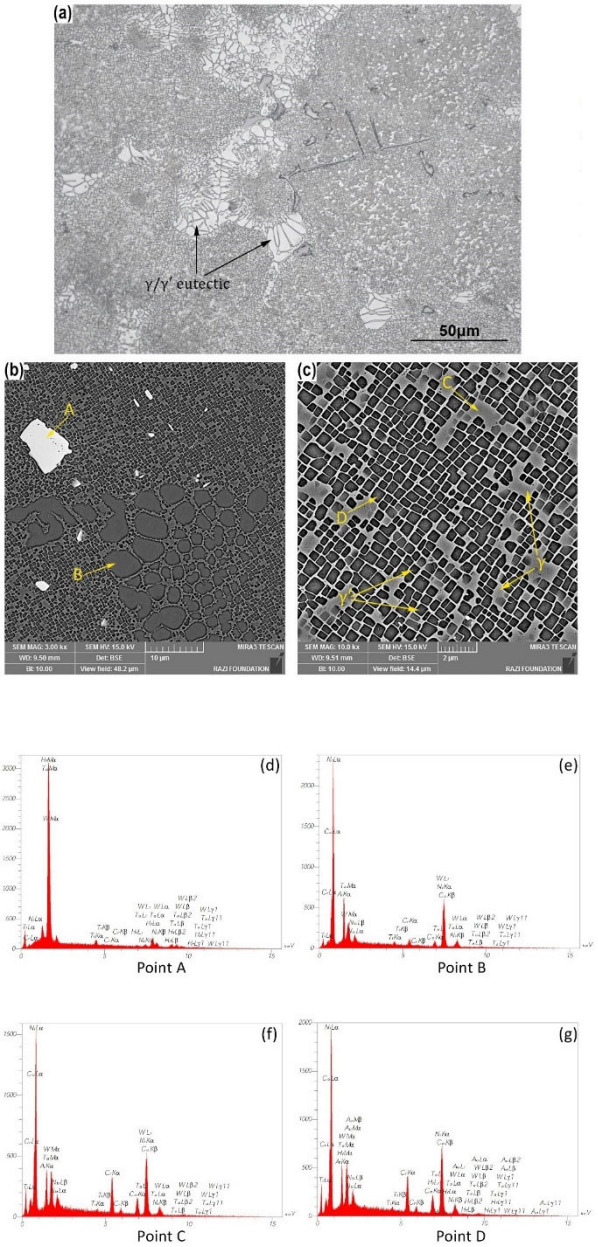

Figure 2. Microstructures of the DS alloy: a) optical micrograph of the microstructure; b) SEM detailed microstructure; c) γ' morphology; d) EDS from point A; e) EDS from point B; f) EDS from point C; g) EDS from point D

2.2 Low Cycle Fatigue Test Procedure

For this study directionally-solidified alloy after the heat treatment procedures was used. The LCF specimens were machined with an extensometer gauge section of 5.75 mm, 27 mm in length. The low cycle fatigue test specimen and facilities are shown in Fig. 3. All specimens used in this study were designed according to ASTM standard E606 because the solidification direction is parallel to the loading axis (along [001] crystal orientation with a misorientation less than ± 15°) and they were machined from casted and heat-treated material. The ratio of the gage section area to the gage section diameter

is a vital factor in ASTM E606 strain-controlled low cycle fatigue test standard, which is obtained by the LCF specimens in this study. All casted specimens had the same conditions and the same casting parameters. Also, before the LCF test, all specimens were polished using SiC sandpaper to eliminate the surface machining defects and marks. Afterward, a visual inspection procedure was carried out to ensure that the residual marks were cleaned for each fatigue specimen. Finally, specimens were cleaned with acetone and dried by air. In this study, the strain-controlled LCF tests were carried out at the two temperature conditions of 600 °C and 800 °C. All tests were carried out using a $100\ kN$ servo-hydraulic machine, where the machine had a low-profile load cell with a resolution of $\pm\ 0.2\ kN$. Two N-type thermocouples with a resolution of $\pm\ 2\ °C$ were welded to the gage section to monitor the temperature gradient. A radio frequency induction system was used to apply heat to the specimen, while a PID controller by using the closed-loop feedback control was kept the LCF specimen temperature. Approximately 2 minutes after the set-point temperature became stable, the LCF tests were started. The RF induction system applied maximum temperature on the gage section of LCF test specimens. The mechanical strain amplitudes were 0.4, 0.6, 0.8, and 1%. Therefore, symmetrical triangular waveform and a constant strain amplitude were kept throughout the totally-reversed loading conditions ($R\ =\ -1$). In each LCF test, temperature and mechanical strain amplitude are different. The strain rates were held constant during loading and unloading slopes. Strain (mm/mm), Force (N), displacement (mm), temperature (°C), and the values of the peak forces were monitored and recorded for each cycle. Subsequently, to determine failure, the stress history was periodically analyzed. Fig. 4 shows the mechanical strain amplitudes and temperatures applied to the LCF tests.

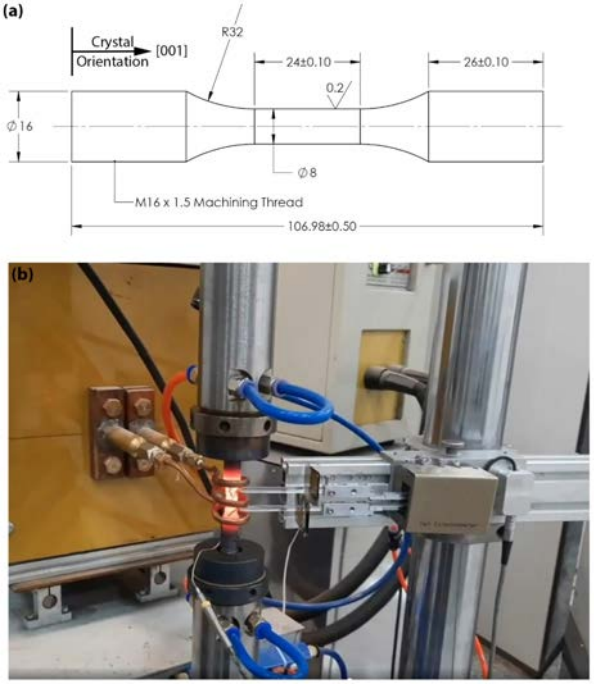

Figure 3. LCF test: a) specimens schematic (in mm); b) test setup

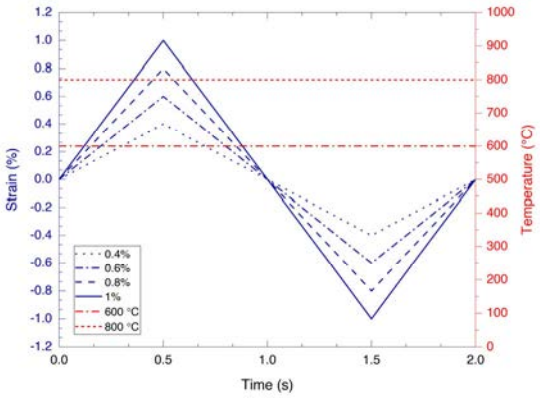

Figure 4. Waveforms and temperatures applied to the strain-controlled LCF tests

3. LOW CYCLE FATIGUE LIFE PREDICTION MODELS

A strain-controlled fatigue curve includes elastic and plastic strain data [34]. In isothermal problems, the Basquin's equation (cyclic stress) and the Coffin–Manson equation (cyclic plastic strain) use the elastic and plastic strain data, respectively [35]. Basquin's equation is more appropriate for high cycle fatigue (HCF) regime [36,37]:

$$\frac{\Delta\varepsilon_e}{2} = \frac{\sigma_f'}{E}\left(2N_f\right)^b \quad (1)$$

Where, σ_f' is the fatigue strength coefficient. On the other hand, the Coffin-Manson equation is used for the low cycle fatigue (LCF) regime and defines the reliance on fatigue life under isothermal loading on plastic strain amplitude [38,39]:

$$\frac{\Delta\varepsilon_p}{2} = \varepsilon_f'\left(2N_f\right)^c \quad (2)$$

Where ε_p is the plastic strain amplitudes, c is the strain ductility exponent, ε_f' is the strain ductility coefficient, and N_i is the cycle to crack initiations. Nevertheless, sometimes in the LCF problems, the Coffin-Manson law has an error in fatigue life prediction, which is assumed because of the unsteady loading condition [40] and unexpected failure modes [41]. As a consequence, the Coffin-Manson equation is not suitable for predicting the lifetime for LCF, when a variable likewise temperature is introduced into the problem [42]. Furthermore, a suitable model for fatigue life prediction has to accurately estimate the material's fatigue life, and it should also be evaluating fatigue properties. Nevertheless, the Basquin equation is suitable for calculating the material's fatigue behavior based on the cyclic stress amplitude, while the Coffin-Manson equation is suitable for assessing the material's fatigue property based on the plastic strain. Therefore, neither of them would be suitable for the evaluation of the integrated fatigue property. Thus, a new model is identified and developed based on hysteresis energy, which is presented below [43]:

$$D_i = \left(\frac{W_i}{W_0}\right)^{\beta} \quad (3)$$

$$D = \sum_{i=1}^{N_f} D_i = \sum_{i=1}^{N_f} \left(\frac{W_i}{W_0}\right)^{\beta} = 1 \quad (4)$$

Where, D_i and W_i are the damage parameter and the hysteresis energy of the i_{th} cycle, respectively. W_0 and b are material constants, and W_0 is the fundamental fatigue toughness. The relation between plastic strain and hysteresis energy is shown in Fig. 5. As can be observed, W_i is the stress-strain hysteresis loop area for each cycle, as shown with the red zone, and the value of $\Delta\varepsilon_p \cdot \Delta\sigma$ is the gray zone. The fatigue damage capacity of the material is defined by W_0. The b parameter is the damage transition exponent. It is described as the ability to transform mechanical work into operative damage to the materials which, in other words, is described as the susceptibility that the damage reacts to the diversity of loading conditions. Moreover, the fatigue damage is denoted by D. In this model, when fatigue damage D equals 1, the material fails. The simplified model is written as follows:

$$D = \sum_{i=1}^{N_f} D_i = \sum_{i=1}^{N_f} \left(\frac{W_s}{W_0}\right)^{\beta} = 1 \quad (5)$$

Where W_s is the half life cycle hysteresis energy, the Eq. (5) can be converted into the Coffin-Manson equation as the following:

$$W_s = W_0 \times N_f^{\frac{-1}{\beta}} \quad (6)$$

However, the $\Delta\sigma/2$, $\Delta\varepsilon_p/2$, and W_S are obtained from the fatigue data.

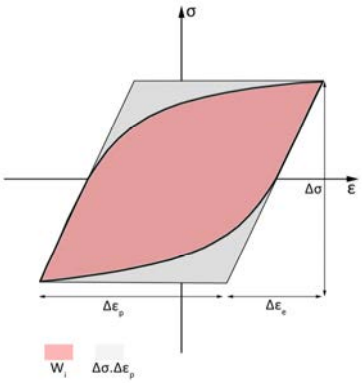

Figure 5. The relation between plastic strain and hysteresis energy

4. RESULTS AND DISCUSSIONS

In this study, based on the LCF test procedure under two temperature conditions of 600 °C and 800 °C, the low cycle fatigue behavior of the DS alloy was investigated. The LCF data achieved by experimental tests at the two temperature conditions are provided in Table 2. The values of stress range amplitude are obtained from the hysteresis curve of the half-life cycle. Based on the obtained data of Table 2, once the strain amplitude is increased, the stress range is increased and the fatigue life (cycle to failure) is decreased.

Table 2. Low cycle fatigue data of the DS alloy tests

Temperature (°C)	*Strain Amplitude (%)*	*Cycle to Failure (N_f)*	*Half-Life Stress Range (MPa)*
600	0.4	30186	1732
600	0.6	4268	1855
600	0.8	2760	2059
600	1	650	2161
800	0.4	3642	1312
800	0.6	844	1454
800	0.8	246	1580
800	1	226	1674

A set of strain-controlled experiments were carried out to evaluate the effect of temperature on the fatigue life under axial loading in the direction along the solidification axis. In the low cycle fatigue, the hysteresis loop (cyclic stress-strain behavior) indicates the connection between the strain and the stress ranges for each cycle. The stress-strain hysteresis curves can be achieved by using the companion method. This method is used to determine the stable cyclic stress-strain of the material throughout the LCF test. The hysteresis loops for LCF tests are plotted in Fig. 6 under two temperature conditions and the mechanical strain amplitudes of 0.4, 0.6, 0.8, and 1 %. As shown in Fig. 6, at the temperature condition of 600 °C, at the strain amplitude of 0.4% the highest stress value decreased from 994 MPa at the first cycle to 831 MPa at the half-life cycle, at the strain amplitude of 0.6% it decreased from 1059 MPa to 880 MPa, at the strain amplitude of 0.8% it decreased from 1144 MPa to 1007 MPa, and the strain amplitude of 1% it declined from 1205 MPa to 1058 MPa. While at 800 °C, at the strain amplitude of 0.4%, the highest stress value decreased from 914 MPa to 655 MPa from the first cycle to the half-life cycle, at the strain amplitude of 0.6% it decreased from 963 MPa to 748 MPa, at the strain of 0.8% it decreased from 1095 MPa to 836 MPa, and at the strain amplitude of 1%, it declines from 1130 MPa to 825 MPa. The hysteresis loops showed the stress value is increased with increasing the strain amplitude, and while the temperature is increased from 600 °C to 800 °C, of all strain amplitudes the temperature-induced softening is observed and the material shows a softening behavior. Therefore, the cyclic stress-strain curves showed that the cyclic softening occurs at both temperature conditions at all the strain amplitudes. A comparison of the experimental results, depicted in Fig. 6, for LCF tests, reveals that the fatigue life is decreased when the temperature shifts from 600 °C to 800 °C for all strain amplitudes. In precipitation-hardened alloys, the occurrence of the cyclic softening behavior depends on some phenomena which are the formation of dislocation networks at the γ/γ' interface, shearing of precipitates, dissolution of precipitates, and coarsening of the precipitates [44,45]. The cyclic stress-strain

hysteresis loops obtained with the experimental test data for two temperature conditions indicated that, at a lower temperature, the material had higher stiffness when the load was aligned along the solidification direction of the material. The width of the hysteresis loop can be used to calculate the plastic strain range (Fig. 5). For an assumed strain amplitude, the plastic strain amplitude increased with increasing temperature from 600 °C to 800 °C.

Based on the hysteresis loops obtained from the experimental test of alloy, the degree of softening is determined using the Eq. (7) as follows [46]:

$$\text{Degree of softening} = \frac{\left(\frac{stress\ range}{2}\ at\ half\ life\ cycle\right) - \left(\frac{stress\ range}{2}\ at\ the\ first\ cycle\right)}{\frac{stress\ range}{2}\ at\ the\ first\ cycle} \quad (7)$$

The degrees of softening at the half-life cycle for all LCF tests are presented in Table 2. The variations of the degree of softening vs strain amplitudes are shown in Fig. 7. For temperature condition of 600 °C, the degree of softening at the strain amplitude of 0.4% to 1% is increased from 18.2% to 23.1%, and for temperature condition of 800 °C, is increased from 20.6% to 39.8%. As can be observed, that through increasing the strain amplitude the degree of softening increased for all strain amplitudes and temperatures, and also, the degree of softening is increased with increasing the temperature from 600 °C to 800 °C.

The cyclic stress amplitude versus the number of cycles is called the cyclic stress response that is a significant parameter in LCF, and describes the stress amplitude at the final stress level, while also showing the deformation throughout the cyclic loading of the material. Cyclic stress response under two temperature conditions for individual strain amplitudes of the directionally-solidified alloy is shown in Fig. 8. Peak stress values are used to show the cyclic stress response of the material. The cyclic stress response showed at both temperature conditions and all the strain amplitudes of the alloy showed a normal cyclic response and by increasing the strain amplitude the cyclic stress amplitude is increased. Throughout the cyclic loading, the material reveals softening behavior until the time when the overload step occurs. As shown in Fig. 8 at all temperatures and the strain amplitudes, curves indicate that by increasing the strain amplitude the cyclic stress amplitude is also increased. For both temperature conditions, the cyclic softening was seen throughout the test process and followed by a rapid decline in the stress due to the initiation of microcracks and their growth leading to failure. Also, at temperature transition from 600 °C to 800 °C, the curves show that the stresses are steadily decreasing. Furthermore, as can be seen, as the softening increases the lifespan would be less. The cyclic stress response hypothesis describes in the materials with a degree of work hardening (σ_{UTS}/σ_{YS} ratio) less than 1.4 cyclic softening is anticipated which is in line with the hypothesis. When gradual strain softening is occurred at the lower temperatures, rapid strain softening at higher temperatures is observed and the degree of work hardening is higher at 800 °C compared with that at 600 °C. In the precipitated hardening superalloys, the dislocation–precipitate interaction mechanisms determine the cyclic stress response behavior. While the principal mechanism is precipitate shearing, the initial hardening is mostly followed by a period of softening, or only softening can be observed.

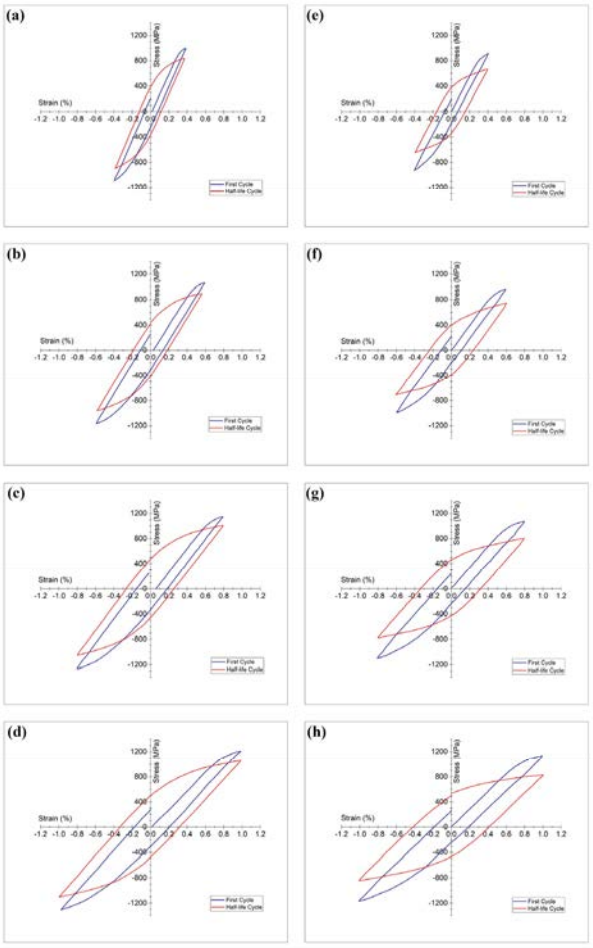

Figure 6. Cyclic stress-strain hysteresis loops of the DS alloy at various temperatures and strain amplitudes: a) 600 °C at 0.4%; b) 600 °C at 0.6%; c) 600 °C at 0.8%; d) 600 °C at 1%; e) 800 °C at 0.4%; f) 800 °C at 0.6%; g) 800 °C at 0.8%; and h) 800 °C at 1%

To predict fatigue life, the Coffin-Manson model, based on plastic deformation and a model based on the hysteresis energy criterion is used. The values of plastic strain amplitudes versus the number of cycles and the hysteresis energy during cyclic deformation for all LCF tests are shown in Fig. 9 (a) and (b) and Fig. 9 (c) and (d) respectively. Fig. 9 (a) and (b) demonstrated that the plastic strain amplitudes increase after a small cycling interval for all strain amplitudes at 600 °C and 800 °C. The results obtained from Fig. 9 (a) and (b) show a monotonic increase in the plastic strain amplitude with the increasing number of cycles, indicating the occurrence of cyclic softening in the directionally-solidified alloy. Based on the obtained results from Fig. 9 (b) and (c), hysteresis energy reveals a similar behavior to that of the plastic strain amplitude.

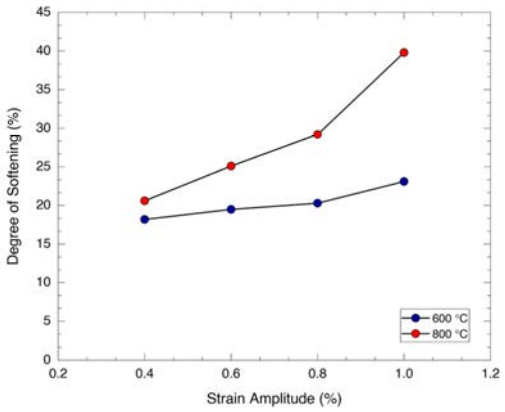

Figure 7. Degree of softening values versus strain amplitudes at two temperature conditions

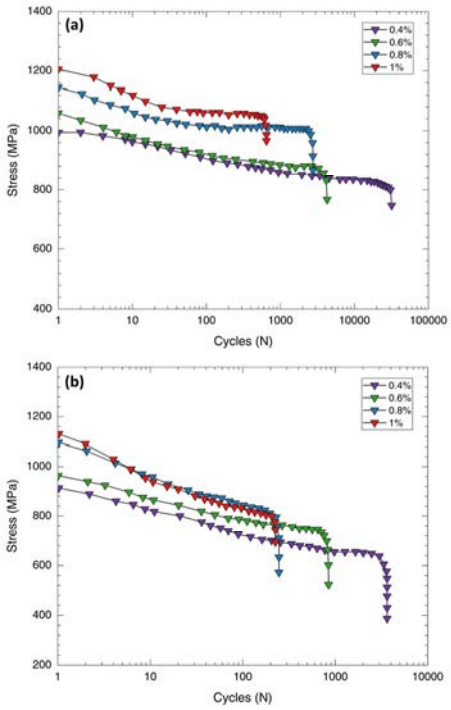

Figure 8. Cyclic stress response curves of LCF tests: a) 600 °C; b) 800 °C

The fitted curves of the low cycle fatigue life prediction models based on the Coffin-Manson equation are plotted in Fig. 10 (a). The values of R^2 are fitted based on the Coffin-Manson equation are 0.90 and 0.94 under 600 °C and 800 °C LCF test conditions, respectively. A comparison of the results of the plastic strain amplitude life model at the two temperature conditions indicates that the fatigue life decreased by temperature transition from 600 °C to 800 °C. The fitted curves of the fatigue life prediction models based on the hysteresis energy model are plotted in Fig. 10 (b). The values of R^2 are fitted based on the hysteresis energy model equation and are obtained as 0.91 and 0.93 under 600 °C and 800 °C LCF test conditions, respectively. This hysteresis energy model shows a good ability to estimate the fatigue life of the LCF mechanism at high-temperature conditions. The plastic strain amplitude-life and hysteresis energy-life at both temperature conditions showed that the fatigue life is decreased by increasing the temperature and strain amplitude.

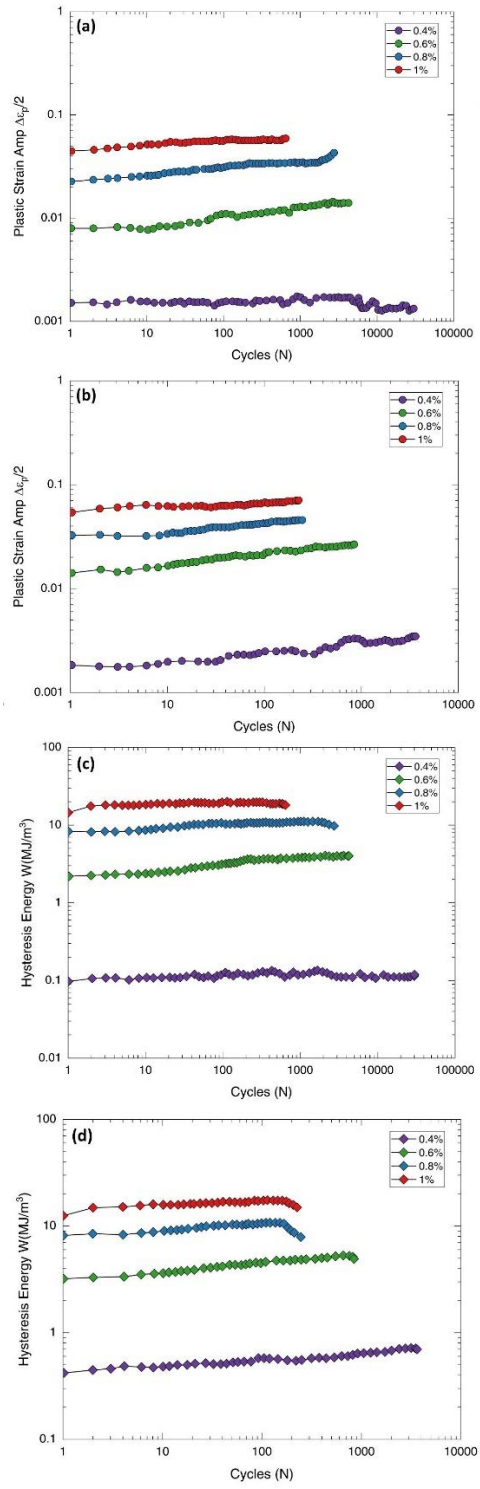

Figure 9. a) Plastic strain amplitude at 600 °C; b) Plastic strain amplitude at 800 °C; c) Hysteresis energy at 600 °C; and d) Hysteresis energy at 800 °C

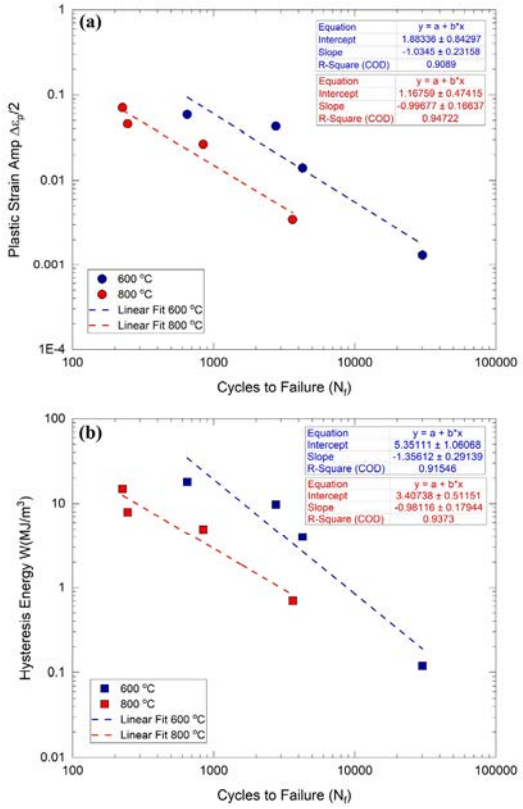

Figure 10. Fatigue life prediction models of two temperature conditions: a) Coffin-Manson equation model; b) hysteresis energy model

5. CONCLUSIONS

The isothermal low cycle fatigue behavior of the directionally-solidified alloy was studied under two temperature conditions of 600 °C and 800 °C. The main conclusions obtained in the current study can be written as follows:

1. Comparison of low cycle fatigue under two temperature conditions of 600 °C and 800 °C showed that the fatigue life decreases with increased temperature from 600 °C to 800 °C.
2. The cyclic hysteresis loops obtained in the experimental tests for two temperature conditions of LCF tests showed that the material had higher stiffness in lower temperatures, and with changing temperature from 600 °C to 800 °C, a cyclic softening was observed.
3. The results of plastic strain amplitude tests showed a monotonic increase in the plastic strain amplitude with the increasing number of cycles, indicating that cyclic softening occurred in the LCF test process.
4. The Coffin-Manson and hysteresis energy models could appropriately predict the low cycle fatigue life under the isothermal LCF test condition.
5. The Coffin-Manson and hysteresis energy models have presented better LCF life prediction results at 800°C conditions in comparison with 600°C.

6. REFERENCES

1. B. Salehnasab, J. Marzbanrad, E. Poursaeidi, Transient thermal fatigue crack propagation prediction in a gas turbine component, Eng. Fail. Anal. 130 (2021) 105781. https://doi.org/10.1016/j.engfailanal.2021.105781.
2. S.S.K. Balam, M. Tamilselvi, A.K. Mondal, R. Rajendran, An investigation into the cracking of platinum aluminide coated directionally solidified CM247 LC high pressure nozzle guide vanes of an aero engine, Eng. Fail. Anal. 94 (2018) 24–32. https://doi.org/10.1016/j.engfailanal.2018.07.027.
3. J.M. Martinez-Esnaola, M. Arana, J. Bressers, J. Timm, A. Martin-Meizoso, A. Bennett, E.E. Affeldt, Crack initiation in an aluminide coated single crystal during thermomechanical fatigue, ASTM Spec. Tech. Publ. 1263 (1996) 68–81. https://doi.org/10.1520/STP16447S.
4. M. Schlesinger, T. Seifert, J. Preussner, Experimental investigation of the time and temperature dependent growth of fatigue cracks in Inconel 718 and mechanism based lifetime prediction, Int. J. Fatigue. 99 (2017) 242–249. https://doi.org/10.1016/j.ijfatigue.2016.12.015.
5. D. Furrer, H. Fecht, Ni-based superalloys for turbine discs, Jom. 51 (1999) 14–17. https://doi.org/10.1007/s11837-999-0005-y.
6. B. Salehnasab, D. Zarifpour, J. Marzbanrad, G. Samimi, An Investigation into the fracture behavior of the IN625 hot-rolled superalloy, J. Mater. Eng. Perform. 30 (2021) 7171–7184. https://doi.org/https://doi.org/10.1007/s11665-021-05895-x.
7. P. Caron, T. Khan, Evolution of Ni-based superalloys for single crystal gas turbine blade applications, Aerosp. Sci. Technol. 3 (1999) 513–523. https://doi.org/10.1016/S1270-9638(99)00108-X.
8. K. Slámečka, J. Pokluda, M. Kianicová, J. Horníková, K. Obrtlík, Fatigue life of cast Inconel 713LC with/without protective diffusion coating under bending, torsion and their combination, Eng. Fract. Mech. 110 (2013) 459–467. https://doi.org/10.1016/j.engfracmech.2013.01.001.
9. R. Rajendran, M.D. Ganeshachar, T.M. Rao, Condition assessment of gas turbine blades and coatings, Eng. Fail. Anal. 18 (2011) 2104–2110. https://doi.org/10.1016/j.engfailanal.2011.06.017.
10. S.K. Bhaumik, M. Sujata, M.A. Venkataswamy, M.A. Parameswara, Failure of a low pressure turbine rotor blade of an aeroengine, Eng. Fail. Anal. 13 (2006) 1202–1219. https://doi.org/10.1016/j.engfailanal.2005.12.002.
11. J.F. Nie, Z.L. Liu, X.M. Liu, Z. Zhuang, Size effects of γ′ precipitate on the creep properties of directionally

solidified nickel-base super-alloys at middle temperature, Comput. Mater. Sci. 46 (2009) 400–406. https://doi.org/10.1016/j.commatsci.2009.03.023.

12. Y. Min, X. Wu, L. Xu, W. Tang, S. Zhang, G. Wallner, D. Liang, Y. Feng, Influence of different surface treatments of H13 hot work die steel on its thermal fatigue behaviors, J. Shanghai Univ. (English Ed. 5 (2001) 326–330. https://doi.org/10.1007/s11741-001-0049-x.

13. R.K. Rai, J.K. Sahu, S.K. Das, N. Paulose, D.C. Fernando, C. Srivastava, Cyclic plastic deformation behaviour of a directionally solidified nickel base superalloy at 850° C: damage micromechanisms, Mater. Charact. 141 (2018) 120–128. https://doi.org/10.1016/j.matchar.2018.04.039.

14. L. Zhang, L.G. Zhao, A. Roy, V. V Silberschmidt, G. Mccolvin, Low-cycle fatigue of single crystal nickel-based superalloy–mechanical testing and TEM characterisation, Mater. Sci. Eng. A. 744 (2019) 538–547. https://doi.org/10.1016/j.msea.2018.12.084.

15. S. Qu, C.M. Fu, C. Dong, J.F. Tian, Z.F. Zhang, Failure analysis of the 1st stage blades in gas turbine engine, Eng. Fail. Anal. 32 (2013) 292–303. https://doi.org/10.1016/j.engfailanal.2013.03.017.

16. B. Salehnasab, E. Poursaeidi, S.A. Mortazavi, G.H. Farokhian, Hot corrosion failure in the first stage nozzle of a gas turbine engine, Eng. Fail. Anal. 60 (2016). https://doi.org/10.1016/j.engfailanal.2015.11.057.

17. S. Kumari, D.V. V Satyanarayana, M. Srinivas, Failure analysis of gas turbine rotor blades, Eng. Fail. Anal. 45 (2014) 234–244. https://doi.org/10.1016/j.engfailanal.2014.06.003.

18. T.J. Carter, Common failures in gas turbine blades, Eng. Fail. Anal. 12 (2005) 237–247. https://doi.org/10.1016/j.engfailanal.2004.07.004.

19. B. Salehnasab, E. Poursaeidi, Mechanism and modeling of fatigue crack initiation and propagation in the directionally solidified CM186 LC blade of a gas turbine engine, Eng. Fract. Mech. 225 (2020) 106842. https://doi.org/10.1016/j.engfracmech.2019.106842.

20. R.I. Stephens, A. Fatemi, R.R. Stephens, H.O. Fuchs, Metal fatigue in engineering, John Wiley & Sons, 2000.

21. B. Salehnasab, J. Marzbanrad, E. Poursaeidi, Conventional shot peening treatment effects on thermal fatigue crack growth and failure mechanisms of a solid solution alloy, Eng. Fail. Anal. 155 (2024) 107740. https://doi.org/10.1016/j.engfailanal.2023.107740.

22. K. Prasad, R. Sarkar, P. Ghosal, V. Kumar, M. Sundararaman, High temperature low cycle fatigue deformation behaviour of forged IN 718 superalloy turbine disc, Mater. Sci. Eng. A. 568 (2013) 239–245. https://doi.org/10.1016/j.msea.2012.12.069.

23. S. Cano, J.A. Rodríguez, J.M. Rodríguez, J.C. García, F.Z. Sierra, S.R. Casolco, M. Herrera, Detection of damage in steam turbine blades caused by low cycle and strain cycling fatigue, Eng. Fail. Anal. 97 (2019) 579–588. https://doi.org/10.1016/j.engfailanal.2019.01.015.

24. H. Gao, C. Fei, G. Bai, L. Ding, Reliability-based low-cycle fatigue damage analysis for turbine blade with thermo-structural interaction, Aerosp. Sci. Technol. 49 (2016) 289–300. https://doi.org/10.1016/j.ast.2015.12.017.

25. D. Gustafsson, J.J. Moverare, S. Johansson, K. Simonsson, M. Hörnqvist, T. Månsson, S. Sjöström, Influence of high temperature hold times on the fatigue crack propagation in Inconel 718, Int. J. Fatigue. 33 (2011) 1461–1469. https://doi.org/10.1016/j.ijfatigue.2011.05.011.

26. S.M. Seo, I.S. Kim, C.Y. Jo, Low Cycle Fatigue and Fracture Behavior of Nickel-Base Superalloy CM247LC at 760° C, in: Mater. Sci. Forum, Trans Tech Publ, 2004: pp. 561–564. https://doi.org/10.4028/www.scientific.net/MSF.449-452.561.

27. S.D. Antolovich, S. Liu, R. Baur, Low cycle fatigue behavior of René 80 at elevated temperature, Metall. Trans. A. 12 (1981) 473–481. https://doi.org/10.1007/BF02648545.

28. Z. He, Y. Zhang, W. Qiu, H.-J. Shi, J. Gu, Temperature effect on the low cycle fatigue behavior of a directionally solidified nickel-base superalloy, Mater. Sci. Eng. A. 676 (2016) 246–252. https://doi.org/10.1016/j.msea.2016.08.064.

29. L. He, Q. Zheng, X. Sun, H. Guan, Z. Hu, K. Tieu, C. Lu, H. Zhu, Effect of temperature and strain amplitude on dislocation structure of M963 superalloy during high-temperature low cycle fatigue, Mater. Trans. 47 (2006) 67–71. https://doi.org/10.2320/matertrans.47.67.

30. W. Deng, J. Xu, Y. Hu, Z. Huang, L. Jiang, Isothermal and thermomechanical fatigue behavior of Inconel 718 superalloy, Mater. Sci. Eng. A. 742 (2019) 813–819. https://doi.org/10.1016/j.msea.2018.11.052.

31. R.J. Kashinga, L.G. Zhao, V. V Silberschmidt, F. Farukh, N.C. Barnard, M.T. Whittaker, D. Proprentner, B. Shollock, G. McColvin, Low cycle fatigue of a directionally solidified nickel-based superalloy: Testing, characterisation and modelling, Mater. Sci. Eng. A. 708 (2017) 503–513. https://doi.org/10.1016/j.msea.2017.10.024.

32. S. Mukherjee, K. Barat, S. Sivaprasad, S. Tarafder, S.K. Kar, Elevated temperature low cycle fatigue behaviour of Haynes 282 and its correlation with microstructure–Effect of ageing conditions, Mater.

Sci. Eng. A. 762 (2019) 138073. https://doi.org/10.1016/j.msea.2019.138073.

33. C.V. Rao, N.C.S. Srinivas, G.V.S. Sastry, V. Singh, Low cycle fatigue, deformation and fracture behaviour of Inconel 617 alloy, Mater. Sci. Eng. A. 765 (2019) 138286. https://doi.org/10.1016/j.msea.2019.138286.

34. K. Harris, G.L. Erickson, R.E. Schwer, MAR-M247 derivations—CM247 LC DS alloy, CMSX single crystal alloys, properties and performance, Superalloys. 1984 (1984) 221–230. https://doi.org/10.7449/1984/SUPERALLOYS_1984_221_230.

35. J.-C. Zhao, J.H. Westbrook, Ultrahigh-temperature materials for jet engines, MRS Bull. 28 (2003) 622–630. https://doi.org/10.1557/mrs2003.189.

36. Y.S. Fan, X.G. Yang, D.Q. Shi, S.W. Han, S.L. Li, A quantitative role of rafting on low cycle fatigue behaviour of a directionally solidified Ni-based superalloy through a cross-correlated image processing method, Int. J. Fatigue. 131 (2020) 105305. https://doi.org/10.1016/j.ijfatigue.2019.105305.

37. D. Radonovich, A.P. Gordon, Methods of extrapolating low cycle fatigue data to high stress amplitudes, 2008. https://doi.org/10.1115/GT2008-50365.

38. B.R. Daubenspeck, A.P. Gordon, Extrapolation techniques for very low cycle fatigue behavior of a Ni-base superalloy, (2011). https://doi.org/10.1115/1.4003602.

39. S. Nagarjuna, M. Srinivas, K. Balasubramanian, D.S. Sarmat, Effect of alloying content on high cycle fatigue behaviour of Cu Ti alloys, Int. J. Fatigue. 19 (1997) 51–57. https://doi.org/10.1016/S0142-1123(96)00041-2.

40. J. Lai, T. Lund, K. Rydén, A. Gabelli, I. Strandell, The fatigue limit of bearing steels–Part I: A pragmatic approach to predict very high cycle fatigue strength, Int. J. Fatigue. 38 (2012) 155–168. https://doi.org/10.1016/j.ijfatigue.2011.09.015.

41. K.V.U. Praveen, V. Singh, Effect of cold rolling on the Coffin–manson relationship in low-cycle fatigue of superalloy IN718, Metall. Mater. Trans. A. 39 (2008) 79–86. https://doi.org/10.1007/s11661-007-9378-0.

42. S. Suresh, Fatigue of materials, Cambridge university press, 1998.

43. R. Liu, Z.J. Zhang, P. Zhang, Z.F. Zhang, Extremely-low-cycle fatigue behaviors of Cu and Cu–Al alloys: Damage mechanisms and life prediction, Acta Mater. 83 (2015) 341–356. https://doi.org/10.1016/j.actamat.2014.10.002.

44. L. Xue, A unified expression for low cycle fatigue and extremely low cycle fatigue and its implication for monotonic loading, Int. J. Fatigue. 30 (2008) 1691–1698. https://doi.org/10.1016/j.ijfatigue.2008.03.004.

45. L. Kang, H. Ge, Predicting ductile crack initiation of steel bridge structures due to extremely low-cycle fatigue using local and non-local models, J. Earthq. Eng. 17 (2013) 323–349. https://doi.org/10.1080/13632469.2012.746211.

46. C.W. Shao, P. Zhang, R. Liu, Z.J. Zhang, J.C. Pang, Z.F. Zhang, Low-cycle and extremely-low-cycle fatigue behaviors of high-Mn austenitic TRIP/TWIP alloys: Property evaluation, damage mechanisms and life prediction, Acta Mater. 103 (2016) 781–795. https://doi.org/10.1016/j.actamat.2015.11.015.

47. J. Miao, T.M. Pollock, J.W. Jones, Crystallographic fatigue crack initiation in nickel-based superalloy René 88DT at elevated temperature, Acta Mater. 57 (2009) 5964–5974. https://doi.org/10.1016/j.actamat.2009.08.022.

48. X.G. Wang, J.L. Liu, T. Jin, X.F. Sun, Y.Z. Zhou, Z.Q. Hu, J.H. Do, B.G. Choi, I.S. Kim, C.Y. Jo, Deformation mechanisms of a nickel-based single-crystal superalloy during low-cycle fatigue at different temperatures, Scr. Mater. 99 (2015) 57–60. https://doi.org/10.1016/j.scriptamat.2014.11.026.

49. W.J. Plumbridge, M.E. Dalski, P.J. Castle, High strain fatigue of a type 316 stainless steel, Fatigue Fract. Eng. Mater. Struct. 3 (1980) 177–188. https://doi.org/10.1111/j.1460-2695.1980.tb01112.x.